IOPscience iopscience.iop.org

Home Search Collections Journals About Contact us My IOPscience

# Increased monolayer domain size and patterned growth of tungsten disulfide through controlling surface energy of substrates

This content has been downloaded from IOPscience. Please scroll down to see the full text.

2016 J. Phys. D: Appl. Phys. 49 325304

(http://iopscience.iop.org/0022-3727/49/32/325304)

View the table of contents for this issue, or go to the journal homepage for more

Download details:

IP Address: 155.246.181.28
This content was downloaded on 22/07/2016 at 20:07

Please note that terms and conditions apply.

J. Phys. D: Appl. Phys. **49** (2016) 325304 (10pp)
doi:10.1088/0022-3727/49/32/325304

# Increased monolayer domain size and patterned growth of tungsten disulfide through controlling surface energy of substrates

**Kyle Godin[1], Kyungnam Kang[1], Shichen Fu and Eui-Hyeok Yang**

Department of Mechanical Engineering, Stevens Institute of Technology, Castle Point on Hudson, Hoboken, NJ 07030, USA

E-mail: eyang@stevens.edu

Received 21 March 2016, revised 9 June 2016
Accepted for publication 22 June 2016
Published 21 July 2016

**Abstract**

We report a surface energy-controlled low-pressure chemical vapor deposition growth of $WS_2$ monolayers on $SiO_2$ using pre-growth oxygen plasma treatment of substrates, facilitating increased monolayer surface coverage and patterned growth without lithography. Oxygen plasma treatment of the substrate caused an increase in the average domain size of $WS_2$ monolayers by 78% $\pm$ 2% while having a slight reduction in nucleation density, which translates to increased monolayer surface coverage. This substrate effect on growth was exploited to grow patterned $WS_2$ monolayers by patterned plasma treatment on patterned substrates and by patterned source material with resolutions less than 10 $\mu$m. Contact angle-based surface energy measurements revealed a dramatic increase in polar surface energy. A growth model was proposed with lowered activation energies for growth and increased surface diffusion length consistent with the range of results observed. $WS_2$ samples grown with and without oxygen plasma were similar high quality monolayers verified through transmission electron microscopy, selected area electron diffraction, atomic force microscopy, Raman, and photoluminescence measurements. This technique enables the production of large-grain size, patterned $WS_2$ without a post-growth lithography process, thereby providing clean surfaces for device applications.

Keywords: TMD, $WS_2$, tungsten disulfide, synthesis, chemical vapor deposition, patterning

S Online supplementary data available from stacks.iop.org/JPhysD/49/325304/mmedia

(Some figures may appear in colour only in the online journal)

## Introduction

Monolayer $WS_2$ has been of interest for the past five years for its semiconducting nature, optical properties, and high environmental sensitivity. With a direct bandgap in the visible spectrum near 2 eV [1–3], $WS_2$, along with other transition metal dichalcogenides (TMDs), has been used for field effect transistors and other semiconductor devices [4, 5] and has also been investigated as a nonclassical light source [6]. These applications require high quality, patterned $WS_2$, two requirements which are at odds as the typical patterning and material transfer techniques reduce the quality of $WS_2$, observed as a reduction in carrier mobility or photoluminescence intensity.

Patterning is usually accomplished by growth followed by optical or electron beam lithography, plasma etching of the sample, and then stripping resist. This patterning requires the spin coating and patterning of a masking layer and later, usually incomplete, removal of that layer. By this process the

[1] These authors contributed equally.

 © 2016 IOP Publishing Ltd Printed in the UK

quality of devices made from these materials can be compromised from contamination [7–13]. Direct patterning through growth without a post-lithography process thus would allow for a reduction of potential contaminants. However, previous reports on patterned growth of TMDs focus on multilayer TMDs [14, 15] and graphene [16–20].

Research on CVD growth of $WS_2$ has focused on controlling growth through choice of precursor, controlling flow rates, growth pressures, growth temperatures, or ramp rates [2, 21–25]. However, growth of monolayer van der Waals materials is closely linked to substrate interactions including substrate surface energy, a consequence of the high surface area to volume ratio of these materials. A pre-growth oxygen plasma treatment of the growth substrate was recently shown to increase average grain size with decreased nucleation density for CVD growth of monolayer $MoS_2$ with submicron grains [26]. In addition, oxygen plasma treatment of substrates improved another van-der-Waals growth, the atomic-layer-deposition of alumina on $MoS_2$ substrates [27].

Though chip-scale growth of $MoS_2$ was demonstrated using low-pressure chemical vapor deposition (LPCVD) as early as 2013 [28–30] and later with $WSe_2$ [31], chip-scale monolayer $WS_2$ growth has only recently been demonstrated on Au substrates [32, 33] and by MOCVD on fused silica and $SiO_2$ substrates [29]. In comparison, $MoS_2$ semiconducting devices have been further developed (including signal mixers, memory devices, logic devices, and photonic devices) [34–39], due to the relative difficulty of growth and exfoliation of $WS_2$. However, $WS_2$ has value over other TMDs for certain applications. $WS_2$ has large spin-orbit band splitting for spintronics applications (426 meV for $WS_2$, 148 meV for $MoS_2$, though exceeded by $WSe_2$ at 456 meV) [40]. The mobility is theoretically higher than other semiconducting TMDs ($MoS_2$ is higher in the experimental literature) [41]. Also, though the broadband sunlight absorption by $WS_2$ is less than other TMDs [42], it has been particularly investigated for photonics due to its high PL efficiency and high exciton binding energy [43–47] including use as a gain medium for lasing [48], chosen over $MoS_2$ or $WSe_2$ for its higher quantum efficiency.

Here we report the effect of pre-growth oxygen plasma treatment on the LPCVD growth of $WS_2$ and exploit that effect for patterned growth of monolayer $WS_2$. We show that oxygen plasma pretreatment of substrates dramatically increases the average crystal grain size of monolayer $WS_2$ CVD growth and encourages monolayer $WS_2$ surface coverage, while slightly reducing the nucleation density. We further demonstrate that control of growth through surface treatment lends itself to directly patterned growth of $WS_2$. We show that increased monolayer growth from $WS_2$ also enables patterned growth of $WS_2$ through patterning the $WO_3$ source material or the growth substrate through etching. We furthermore demonstrate multi millimeter scale growth of predominantly monolayer $WS_2$ on an oxidized silicon substrate using the increased surface energy from a pre-growth oxygen plasma treatment.

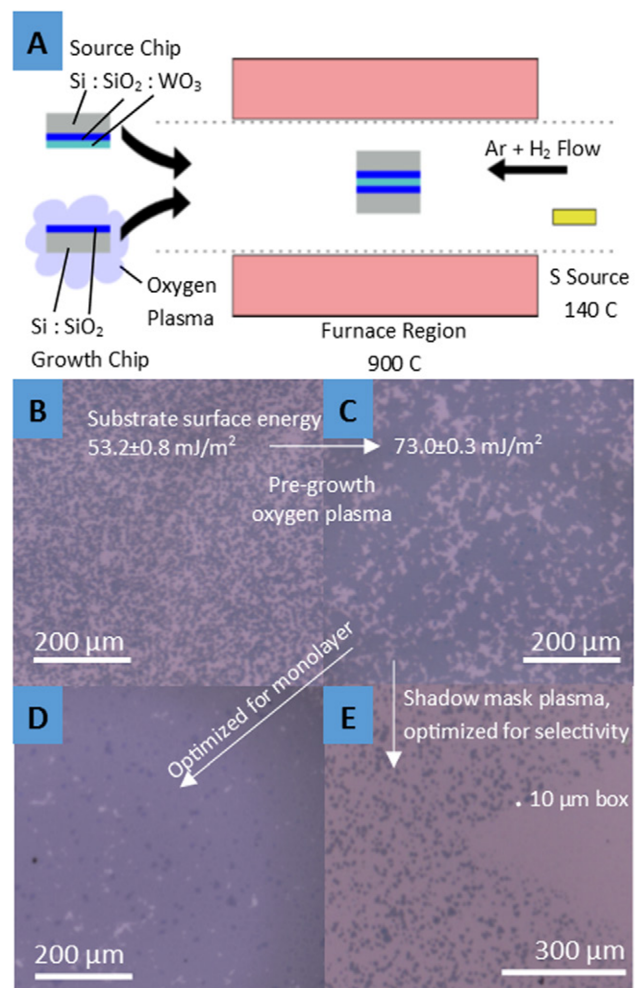


**Figure 1.** CVD growth setup and growth of $WS_2$ with or without $O_2$ plasma. (A) Furnace setup: a $WO_3$ source substrate is placed face to face with a growth substrate in the center of the furnace. Ar, $H_2$, and S are delivered from upstream. (B) and (C) are optical images of different growth chips run concurrently, (B) with no substrate pretreatment and (C) with 3 min of oxygen plasma, increasing the average crystal size by 78% while decreasing nucleation density by 8%. The lighter regions are bare $SiO_2$, the darker purple are monolayer $WS_2$, and the darkest blue are thick $WS_2$ (verified using Raman and PL measurements). (D) Shows a plasma treatment growth optimized for monolayer coverage while (E) shows growth with a shadow mask patterned pre-growth plasma treatment.

## Results and discussion

Growth of $WS_2$ monolayers was performed in an MTI 1200X one-zone split-top furnace with a 3 inch quartz tube, run with a 36 mTorr base pressure and a few hundred mTorr operating pressure when fed with Ar and $H_2$ gas and S vapor evaporated from molten S (illustrated in figure 1(A)). The maximum temperature was 900 °C but growth interruption experiments show that growth occurred during the ramping process from 815 °C to 900 °C and after reaching 900 °C. The samples were unloaded when the furnace cooled to under 40 °C. The total time including cooling, from loading to unloading the samples, was 3 h. Growth substrates were 1 cm × 1 cm chips with

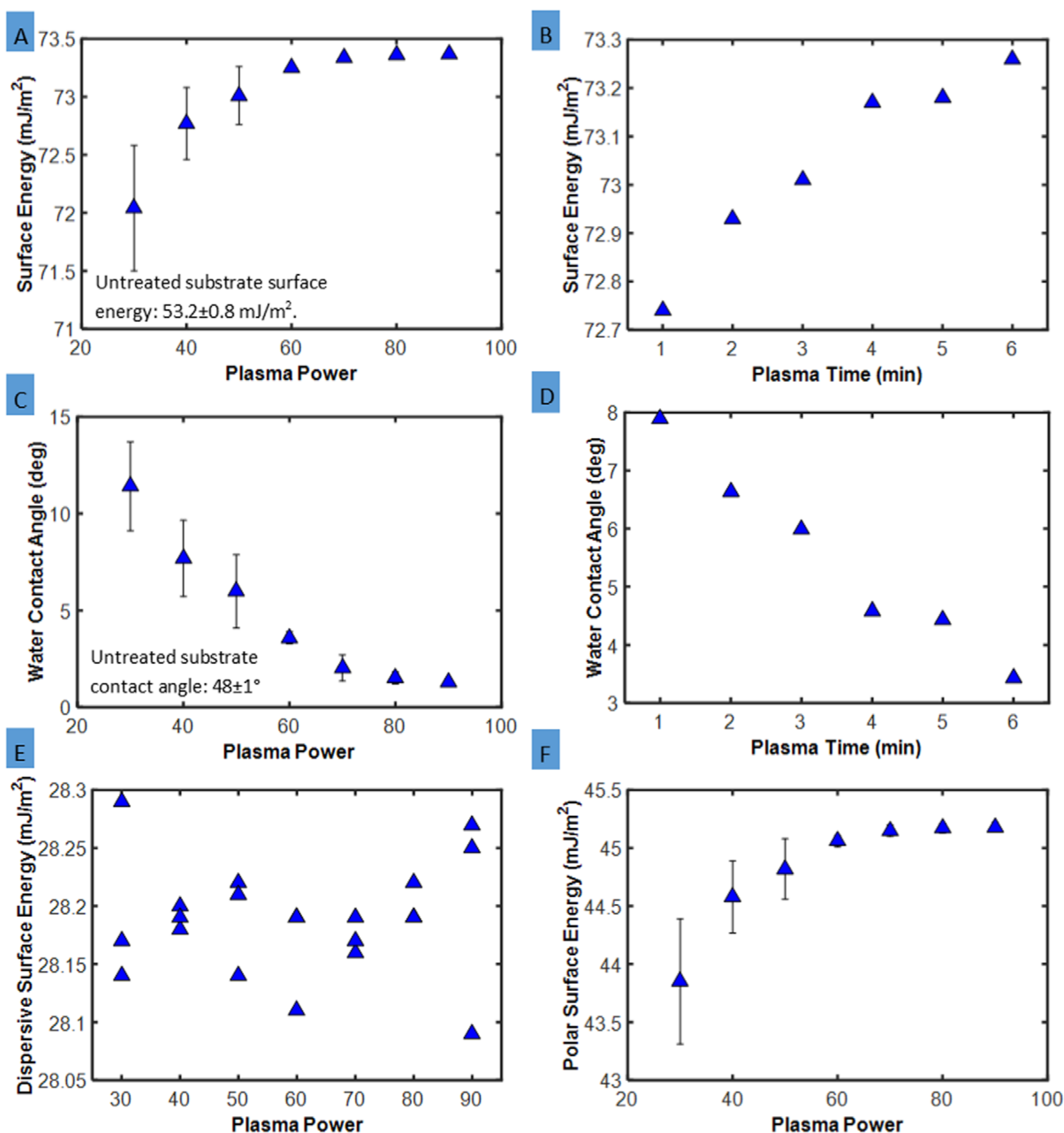


**Figure 2.** Contact angle-based Owens–Wendt surface energy measurements of plasma treated substrates using toluene and water. The untreated substrate showed a contact angle of $48 \pm 1°$ and surface energy $53.2 \pm 0.8$ mJ m$^{-2}$. (A) Surface energy versus plasma power. (B) Surface energy versus plasma time. (C) Water contact angle versus plasma power. (D) Water contact angle versus plasma time. (E) and (F) illustrate that the increase in surface energy is attributed to a polar component, consistent with formation of silanol groups on the surface.

90 nm $SiO_2$ on Si ('growth chips') and were placed face to face with other chips ('source chips') which were covered with 5 nm of evaporated $WO_3$. For oxygen plasma assisted growth, the growth substrates were exposed to plasma directly before growth (details in Methods). After growth, the $WO_3$ source substrate was covered with thick, nonuniform $WS_2$ (figure S1 (stacks.iop.org/JPhysD/49/325304/mmedia)) while the target substrate was covered in predominantly monolayer $WS_2$ (figures 1(B)–(E)).

Pre-growth oxygen plasma treatment was found to increase the crystal size of the monolayer $WS_2$ while causing a smaller, negative effect on the nucleation density. A representative run of $WS_2$ chips with and without oxygen plasma treatment grown simultaneously is shown in figures 1(B) and (C). The untreated substrate had a nucleation density of $940 \pm 15$ crystals mm$^{-2}$ and an average $WS_2$ crystal size of $56 \pm 1$ $\mu$m$^2$. With plasma treatment, the nucleation density decreased by 8% to $871 \pm 11$ crystals mm$^{-2}$ while the average $WS_2$ crystal sized increased by 78% to $101 \pm 2$ $\mu$m$^2$. By optimizing the growth, a continuous $WS_2$ film which is predominantly polycrystalline monolayer (up to multi-mm$^2$ in size) can be obtained (figure 1(D)). Additional characterization of the large area growth appears in figure S2. The percentage increase in domain size between treated and untreated samples is given as a representative example as it is sensitive to the growth recipe, an order of magnitude difference being possible. For example, the patterned growth in figure 1(E) has separated monolayer growth in the plasma treated region

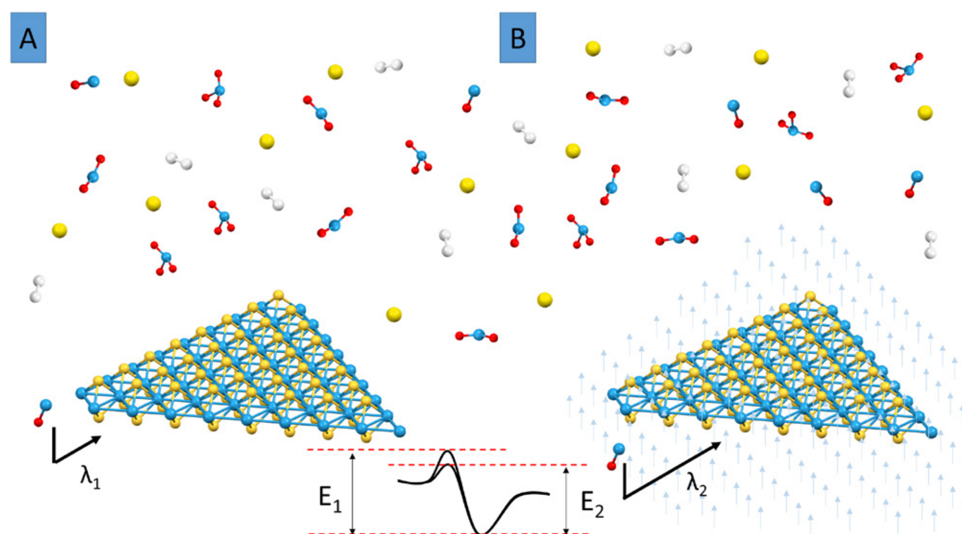


**Figure 3.** Growth kinetics of $WS_2$ with oxygen plasma surface treatment. Growth on an untreated, low energy substrate is shown on the left (A) and on a plasma treated substrate on the right (B). The vertical arrows serve to illustrate the higher energy of the surface. In the vapor phase are shown $H_2$ gas (white), S vapor (yellow) and various W oxides (blue and red). Drawn are qualitative representations of the longer surface diffusion length $\lambda_2$ and lower activation energy $E_2$ than the plasma treated substrate.

and almost no growth in the untreated region. To produce the patterned growth in figure 1(E), (a) contact shadow mask was used during the plasma treatment process; the mask was removed before growth leaving only the surface energy difference to do the patterning. The growth in figure 1(E) was run with process parameters optimized for selectivity between the plasma treated and untreated regions, while avoiding multilayer growth in the plasma treated regions. Polished Si and rolled Cu shadow masks both resulted in well-defined patterns, suggesting that one can use any mask which conforms to the substrate and resists the oxygen plasma treatment process. Polymer masks redeposited on the exposed regions during the plasma treatment and became nucleation sites favouring multilayer $WS_2$ growth.

Grain size measurements on the grown $WS_2$ monolayers were performed by exposing the sample in ambient conditions to oxidize the crystal at the grain boundaries over an approximately 7 d period (figure S3), then taking optical microscope images and analysing using the Particle Analysis plugin of ImageJ [49]. In order to measure average grain sizes, optical images of the same region were taken before and after oxidizing the sample with the total area of monolayer $WS_2$ taken from the un-etched samples and the number of grains counted using the second image when the grain boundaries were revealed by oxidation. The correspondence of the oxidation with the grain boundaries has been established by several reports [22, 23, 50], which also showed that the grain boundaries can also be revealed by heating the sample on a hot plate in air in 20 min [22] or by UV treatment in humid atmospheres [50].

To elucidate the effect of oxygen plasma on growth and to inform the growth model, we performed surface energy measurements of plasma treated samples. The surface energy was found by performing contact angle measurements and fitting to the Owens–Wendt model which divides the surface energy into polar and dispersive components [51]. Toluene was used as a purely dispersive liquid and water as a strongly polar liquid. After plasma treatment for 1–6 min with powers 30–90 W, the surface energy of the untreated state jumped from a surface energy of $53.2 \pm 0.8$ mJ $m^{-2}$ (water contact angles $48 \pm 1$) into the range 71–73 mJ $m^{-2}$ (water contact angles 1–13°) (figures 2(A) and (B)). While surface energy increased 74% compared to untreated substrates, the variation in surface energy was only 3% for the experimental parameters 1–6 min and 30–90 W. Higher powers and longer times (5 min, 100 W) resulted in reduced grain size and increased percentage of thick growth of $WS_2$ (figure S4). The small variation in surface energy despite a noticeable trend in water contact angle (figures 2(C) and (D) is due to the contact angle appearing in a cosine. Though difficult to measure contact angles less than a few degrees using the sessile drop method, the error on the surface energy is only $\pm 0.04$ mJ $m^{-2}$ for a contact angle range of 0.1–2°, so errors of measurement on low angles do not affect the conclusions. Figure 2(E) shows how the toluene contact angle and thus the dispersive surface energy does not depend on the plasma power, while figure 2(F) shows how polar component of the surface energy increasing monotonically with plasma power.

The existence of silanol groups on treated surfaces has been experimentally verified through pH dependent contact angle [52] and XPS measurements [53]. Polar-dispersive contact angle measurements on $H_2O$ plasma treated mica showed the same polar-only trend as the experiments presented here and correlated the result with XPS measurements of OH groups [53]. Several experiments and simulations correlate contact angle with surface silanol density [54, 55]. Though several studies support contamination removal as the mechanism for contact angle reduction without reference to surface bonds or silanol groups [56, 57], it is unclear how pure contamination removal would result in a polar surface and be as rapid as we observed. Increased roughness could reduce contact angle, based on the Wenzel model, or could

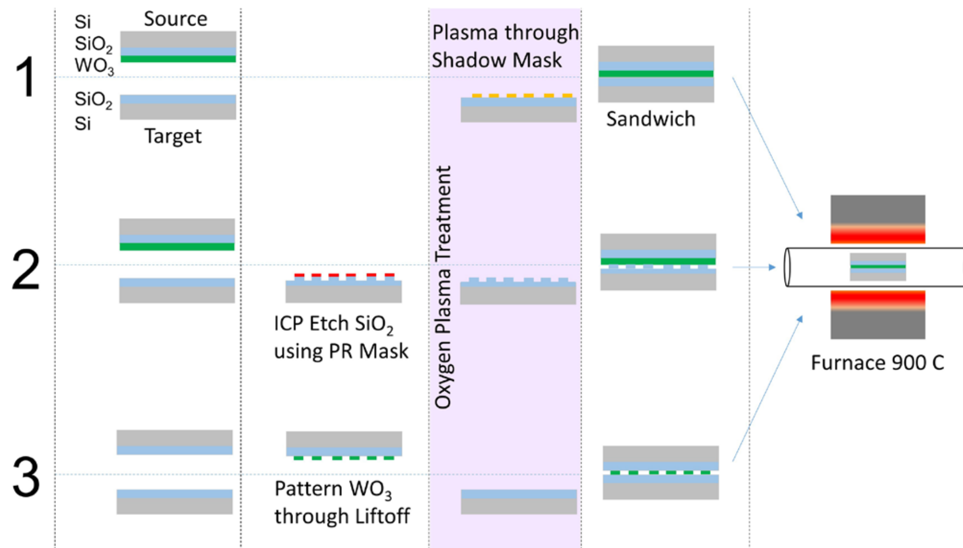


**Figure 4.** Three process flows for patterned growth of monolayer $WS_2$. Each process begins with source and growth substrates, subjects them to different processes, then sandwiches them together for growth. In process 1, the growth substrate is treated to oxygen plasma through a shadow mask. In process 2, the glass surface of the growth substrate is etched in a pattern using $CHF_3$ plasma. In process 3, the source $WO_3$ material on the source substrate is patterned using liftoff while the growth substrate is unpatterned.

provide more surface area for silanol group attachment [58]. In our experiments, surface roughness measurements showed an RMS roughness less than our tool's measurement limit of 0.5 nm for both untreated and treated samples, in agreement with others' measurements of less than 1 nm roughness after 20 min in a high power system [59]. The effect cannot be entirely excluded, but it would be based on sub-nm roughness. The increase of polar surface energy without a change in surface roughness is consistent with the formation of silanol groups on the $SiO_2$ surface. The largest increase in surface energy, from 53 to 72 mJ $m^{-2}$, was rapid, with an additional 3% increase to 73.5 mJ $m^{-2}$ over several minutes or with higher powers. In the first minute adsorbed water and organic contaminants are likely removed and replaced with silanol groups. Simple contaminant removal is not expected to be so rapid, resulting in a polar surface. The additional effect over several minutes cannot be explained by the same short term desorption mechanism, but could be explained by etching of organics or surface reconstruction.

Increased grain size was observed for samples that had rested for up to 30 min before loading, but the best results were obtained from those loaded as quickly as possible (3–5 min) and ramped rapidly to the growth temperature (18 deg $min^{-1}$). Rapid heating above this rate caused poor growth, attributed to overheating the substrates due to the furnace design causing radiative heat transfer from the coils.

The effect of plasma pretreatment on the growth mechanism is illustrated in figure 3. In order to explain the range of results observed we deduce that both the activation energies for nucleation and growth are reduced and the surface diffusion length of the reaction product is increased. This means that the growth is highly dependent on the local supersaturation which explains the wide range of results we observed. Figure 3(A) shows growth kinetics for an untreated surface and figure 3(B) shows a treated surface. Illustrated in the vapor phase are various W oxides, S vapor, and $H_2$ gas which participate in the reaction (Ar carrier not shown and concentrations taken as the same in figures 3(A) and (B)). Pure W is not shown in the vapor phase as it is not volatile at the growth temperature, though the W suboxides are known to be volatile at those temperatures. $H_2$ or $H_2O$ react to reduce the W oxides as part of the reaction; in our experiments there is no $WS_2$ growth from $WO_3$ in a $H_2$ and $H_2O$ free atmosphere. The growing crystal forms bonds between the existing crystal and the substrate which both contribute to the interfacial energy and thus the activation energy. The increased interfacial energy should result in a decreased activation energy for both lateral crystal growth and nucleation, however we observed decreased nucleation density, which can be explained by deconstructing the free energy driving nucleation ($\Delta g$) into the supersaturation $\sigma$ and interfacial energy $\alpha$. The nucleation rate is proportional to the exponential of the free energy [60],

$$\text{Nucleation rate} \propto e^{-\Delta g / kT}$$

where $\Delta g$ is the free energy, $k$ is the Boltzmann constant, and $T$ is the temperature. Here, the free energy is related to the supersaturation and interfacial energy by

$$-\Delta g / kT \propto -\frac{\alpha^3}{\sigma^2}$$

where $\sigma$ is supersaturation and $\alpha$ is interfacial energy. Thus, a decrease in interfacial energy has a strong effect on both the crystal growth rate (and ultimate size) and on the nucleation density. We conclude that a second effect must come into play to reduce the nucleation density. An increase in surface diffusion length is a plausible explanation. The high energy of the surface lowers energy barriers for surface diffusion, increasing the surface diffusion length and consequently decreasing the nucleation density. When reactants arrive at the growing crystal interface they are more easily incorporated due to the lower surface activation energies.

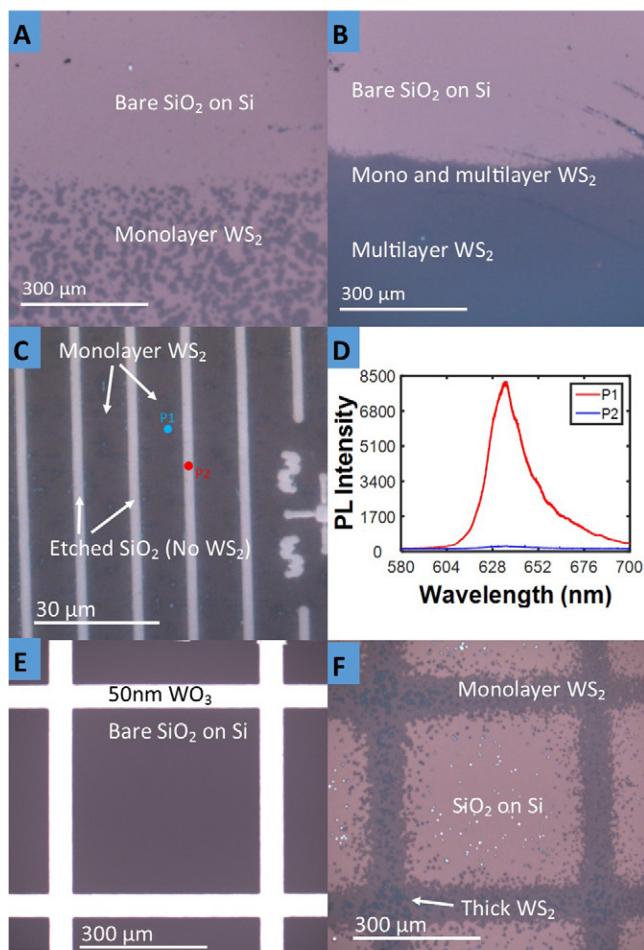


**Figure 5.** Patterned growth using oxygen plasma. Through tailoring the growth process and patterning either the surface energy, source, or substrate, $WS_2$ crystals can be selectively grown. (A) $WS_2$ growth in line and notch patterns using a shadow mask during oxygen treatment. (B) Shadow masked growth of thick, continuous $WS_2$. (C) Patterned growth on a substrate which has been etched by $CHF_3$ plasma with PL characterization in (D). (E) An optical image of the $WO_3$ precursor patterned using liftoff and (F) shows the resulting monolayer growth which matches the precursor pattern on the source substrate.

The supersaturation, which correlates to local reactant concentrations, is a parameter which is highly local and drives the relative importance of the surface diffusion length and the activation energy. This interplay between the two effects results in a high variability between samples which have an increase in grain size and a lower nucleation density and other samples which show both a high increase in nucleation density and a high increase in grain size, as is seen in some of the patterned growth results exhibited in this paper.

Controlling growth by substrate preparation lends itself to patterned growth of monolayer $WS_2$ by promoting growth only in certain areas. Here we demonstrate directly grown, patterned $WS_2$ through three methods (figure 4). In the first method, patterned growth resulted from directly controlling the local surface energy of the substrate by exposing the growth substrate to oxygen plasma pretreatment through a shadow mask. Shadow masks were made from both polished Si and rolled Cu foils. In this case, the chip carrying the $WO_3$ source material was not treated or modified. The result was already shown in figure 1(E) using a triangular mask made from polished Si; figure 5(A) shows the result from a square Si mask and figure 5(B) shows the result at the edge of a region patterned using a Cu foil disk. The differences between figures 5(A) and (B) stem not from the mask but from different growth process parameters. Figure 5(B) had higher sulfur concentration during growth. By selecting appropriate process parameters, either disconnected $WS_2$ monolayers can be grown (figures 1(E) and 5(A)) or connected, few-layer $WS_2$ can be grown (figure 5(B)). In our experiments, the mask material did not affect the growth results as long as the mask conformed well to the substrate (using polished or rolled masks without wrinkles), and could withstand the oxygen plasma treatment. In figures 5(A) and (B) the interface region is sharp, with a transition region smaller than 10 $\mu$m.

The addition of a pre-growth plasma treatment to the process increased the monolayer $WS_2$ coverage from partial coverage and separated triangular crystals to a continuous polycrystalline monolayer $WS_2$ film. The growth chip was patterned by ICP etching in $CHF_3$ plasma using a photoresist mask followed by resist stripping using acetone (55 nm deep in a 90 nm oxide). The growth chip was exposed to oxygen plasma before growth while the $WO_3$ source chip was not modified. Figure 5(C) is an optical image of the result, with continuous polycrystalline monolayer $WS_2$ films separated by regions devoid of $WS_2$ growth, confirmed by photoluminescence data (figure 5(D)). The grown monolayer $WS_2$ has a PL/Raman intensity ratio of 20 while P2 has a ratio of approximately 1. The decreased PL intensity is an indication that there is either no $WS_2$ or thick (>3 layer) $WS_2$ [2], and optical and SEM investigation shows there is no $WS_2$ in the etched trenches (P2). The existence of a Raman signal in P2 is attributed to the probe spot size being near the same size as the features, so signal is picked up from the neighboring monolayer $WS_2$.

Furthermore, oxygen plasma treatment caused nucleation and growth of monolayer $WS_2$ near the $WO_3$ source material, enabling patterned $WS_2$ growth from patterned $WO_3$. The $WO_3$ source material on the source substrate was patterned using lift-off and electron beam evaporation of 50 nm $WO_3$ from pellets. The growth substrate was unpatterned but was still subjected to the oxygen plasma treatment. Figure 5(E) depicts an optical image of the patterned $WO_3$ before growth and figure 5(F) shows the resulting $WS_2$ growth. While polycrystalline monolayer follows the pattern, thicker $WS_2$ appears near the center of the $WO_3$ source strip and at the intersections. In figure 5(F), The 50 $\mu$m $WO_3$ lines expanded to approximately 100 $\mu$m of monolayer $WS_2$ growth. Without oxygen plasma treatment, the growth process resulted in randomly distributed triangular monolayer crystals.

The growth method of contacting the substrates face to face was key to our patterning results, which we attribute to its role in limiting diffusion of W source material. $WS_2$ growth behaves fundamentally differently than Mo-based growth such as $MoS_2$ because both the $WO_3$ and suboxides ($WO_{2.9}$, $WO_{2.72}$, and $WO_2$ are all stable oxides) will

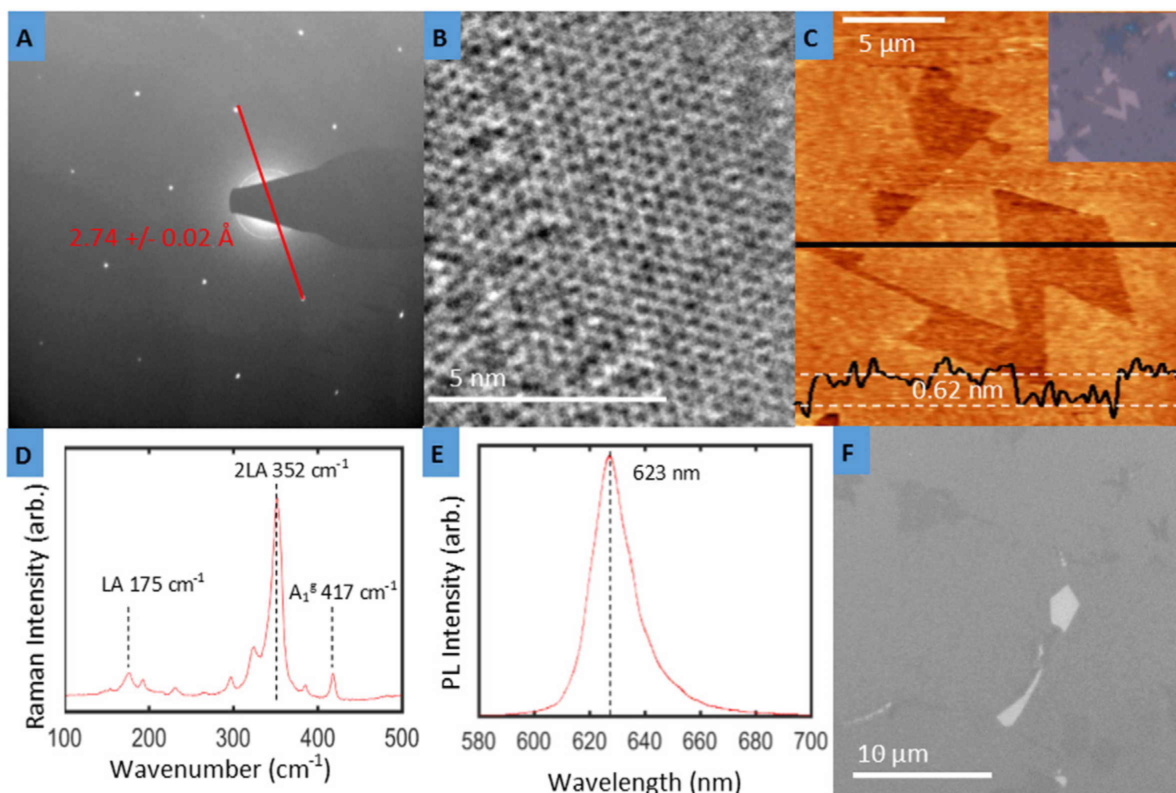


**Figure 6.** Characterization of oxygen-plasma treatment assisted growth. (A) SAED pattern showing well crystallized monolayer $WS_2$ with a lattice spacing of $2.74 \pm 0.02$ Å. (B) HRTEM image showing the $WS_2$ hexagonal lattice with $1.85 \pm 0.03$ Å side length. (C) An AFM image of a void within a polycrystalline $WS_2$ region, shown monolayer by the 0.62 nm step height. (D) WS2 Raman spectrum and (E) PL spectrum. The PL/Raman peak intensity ratio is 102. The strength of the PL signal implies it is a high quality monolayer sample, (F) is an SEM micrograph of a connected growth region.

not melt at the typical growth temperatures (below 900°C). In a non-reducing atmosphere $WO_3$ is completely stable at those temperatures. The suboxides are much more volatile than $WO_3$ at the growth temperatures, with volatility starting around 700 °C and sharply increasing around 900 °C [61]. Thus, growth of $WS_2$ and transport of the W source must occur by vapor phase transport of the suboxides. In the W system, both H and $H_2O$ are known to dramatically reduce the temperature at which suboxides sublimate [26], which means those two have a large effect on CVD $WS_2$ growth. In our experiments, H gas is required to see any growth of $WS_2$ at 900 °C or below, and $H_2O$ contamination actually improves growth to a point, though too much $H_2O$ will damage grown $WS_2$. Because it does not melt, in the W system the amount of $WO_3$ source material does not affect the resulting crystal thickness as much. With patterned $WS_2$ growth, 50 nm $WO_3$ layers were typically used which is a larger amount of material than is needed to grow monolayers. As monolayer growth results from this thick layer, the sublimation of deep W source material is blocked by the top layers, with remaining material visible on the source substrate after growth using optical microscopy. Thus the reaction is limited by time and the amount of sulfur source which makes controlling the sulfur source during $WS_2$ growth critical.

Figure 6 characterizes $WS_2$ growth using oxygen plasma pretreated substrates. Figure 6(A) is a single area electron diffraction (SAED) pattern (TEM model FEI CM 20) from a $WS_2$ monolayer, grown on a plasma treated substrate and transferred to a lacey carbon grid. The sharp points in a six-fold pattern confirm the monolayer nature of the $WS_2$ growth and the high crystallinity. The lattice spacing is measured to be $2.74 \pm 0.02$ Å, in agreement with reported values [23]. Figure 6(B) is an aberration corrected HRTEM image (Jeol JEM2100F at Brookhaven National Lab) showing the hexagonal lattice of $WS_2$ with a hexagon side length of $1.85 \pm 0.03$ Å, in agreement with literature and with the expected value of 1.836 Å from the $WS_2$ crystallographic file 591003.cif from the Crystallographic Open Database [62]. For HRTEM, we observed both hexagonal lattices and triangular lattices (supplementary figure S5). Both types of lattices have been reported for confirmed monolayer $WS_2$ (hexagons [2, 23] and triangles [21–23]). Figure 6(C) is an AFM scan of a void surrounded by polycrystalline $WS_2$, with an optical image inset. The step height from the substrate to the $WS_2$ was 0.62 nm, averaged over many lines, supporting the conclusion that the $WS_2$ is monolayer and supporting our use of optical contrast to identify monolayers in many samples. Typical Raman and photoluminescence spectra from our $WS_2$ samples are shown in figures 6(D) and (E). Spectra were taken on a Horiba Xplora at an excitation wavelength of 532 nm and 16 $\mu$W. The tallest Raman peak is the 2LA peak at 352 nm which subsumes the $E^1_{2g}$ peak; the $A_{1g}$ peak is visible at 417 nm, which indicates the existence of $WS_2$ in agreement with the literature [63]. The PL spectrum was fit by a Gaussian–Lorentzian and appears at

623 nm (1.99 eV) in figure 6(E). Amongst different samples we have observed PL peak energies ranging from 621 nm to 641 nm (2.00 eV–1.94 eV) (figure S6) which agrees with the range observed by other research groups [2, 3]. Raman and PL spectra were taken in a single scan, with PL peak/Raman 2LA peak intensity ratios ranging from 80 to 150, indicating that the sample is monolayer [25]. Figure 6(F) is an SEM image of a connected growth region grown from oxygen plasma. SEM analysis reveals the existence of generally clear monolayer grain surfaces with bilayers appearing mostly at grain boundaries and more rarely over the interior of a grain. These bilayers appear at a similar density in samples grown with or without oxygen plasma (figure S7).

Taken together, the evidence suggests that the $WS_2$ grown on plasma treated substrates is the same quality as on non-plasma treated substrates. If the $WS_2$ resulting from oxygen plasma treatment had a higher defect density, the result would be seen in a decreased PL intensity and the possible appearance of the charged trion peak which is visible at room temperature [12]. Strain or substrate interactions could shift the Raman peaks, which was not seen in our samples. Possible inclusion of oxide defects into the crystal could not be detected using EDX due to the signal being obscured by the oxygen content of the $SiO_2$ substrate.

## Conclusions

We have demonstrated that oxygen plasma pretreatment of $SiO_2$ substrates increases the average grain size and surface coverage for CVD growth of monolayer $WS_2$. The proposed growth model was consistent with the range of observations required both lowered activation energy for growth and increased lateral diffusion on the substrate. The polar surface energy increase from oxygen plasma treatment was ascribed to desorption of surface water and organics, and the formation of silanol groups. The reaction products were verified through HRTEM, SAED, Raman, AFM, and photoluminescence techniques. Through Raman and photoluminescence spectroscopy, $WS_2$ was found to be the same quality whether grown on untreated substrates, oxygen plasma treated substrates, or patterned substrates. Furthermore, oxygen plasma treatment of substrates was shown to improve the results of growth-patterned $WS_2$. Patterned growth of polycrystalline $WS_2$ monolayers resulted from three distinct methods: using a contact shadow mask during plasma treatment, by prepatterning the growth substrate, and by patterning the source material. An improved CVD synthesis route such as presented here, using plasma-prepared growth substrates and contact between the source and growth substrates, could spur development of $WS_2$ devices which rely on high quality, large area or patterned materials. Directly patterned growth of $WS_2$, enabled by growth substrate pretreatment, is a possible avenue towards high quality devices without contamination from transfer or patterning processes.

## Methods

### Growth

An MTI 1200X 1-zone furnace with a 3″ diameter quartz tube was loaded in the center with 0.5–1 cm target substrates with matching size source substrates (5 nm $WO_3$ on 90 nm $SiO_2$ on 500 $\mu$m Si) facing down, in contact. A graphite crucible with 0.8 g of powdered S (Sigma-Aldrich) was placed 10.1 cm outside of the furnace region, in the quartz tube. Two Aalborg MFCs delivered Ar at 40 sccm and $H_2$ at 60 sccm from 700 °C while ramping until 560 °C while cooling. A Welch 8907 pump created a base pressure of 36 mTorr. The temperature was programmed to wait 5 min, ramp at 18 deg $min^{-1}$ to 700 °C, then ramp at 5.8 deg $min^{-1}$ to 900 °C, wait at 900 °C for 25 min, then turn off the heater. The furnace cooled naturally to 560 °C at which point the gases were turned off and the furnace split open for rapid cooling.

### Oxygen plasma treatment

Chips were placed face up in the chamber center of a PlasmaEtch PE-50 system operating at 13.56 MHz. The chamber was pumped to 130 mTorr, flushed with $O_2$ for 3 s, then pumped to the tool base of 88 mTorr. $O_2$ flowed at 15 sccm for 20 s to stabilize before plasma ignition. After the treatment the chamber was flushed with air and pumped to 130 mTorr before venting. Plasma times/powers used were 1–6 min and 30–100 W.

### Transfer

$WS_2$ grown on $SiO_2$ was coated with a thin layer of PMMA 950 A4 using a dropper, then heated at 180 °C for 5 min to drive off the solvent. The chips were floated in 30% KOH (aq); after 20–40 min the Si chip fell to the bottom leaving the PMMA + $WS_2$ square floating on the surface. The PMMA was cleaned in filtered DI water and blown dry with room temperature air. The PMMA + $WS_2$ was successfully transferred to new $SiO_2$ substrates and lacey carbon TEM grids by placing the square $WS_2$ side down and removing PMMA by annealing at 400 °C for 30 min under 200 mTorr vacuum in an MTI OTF 1200X compact furnace with a 2″ quartz tube.

### Characterization

Raman and PL measurements were taken with a Horiba Xplora system with an Andor iDus 420 detector. HRTEM images were taken with a Jeol JEM2100F at Brookhaven National Lab. SAED patterns were taken with an FEI CM 20 TEM in the Laboratory for Multiscale Imaging at Stevens. Roughness measurements were done using a Nanonics MV2000 AFM system with glass fiber tips and AFM data analyzed using WSxM [64]. Surface energy measurements were performed using a Ramé-Hart 250 goniometer by fitting 1–3 $\mu$l drops as circular caps and finding the contact angle, then fitting the contact angles of Toluene (purely dispersive surface tension 28.5 mJ $m^{-2}$) and water (dispersive 21.8 and polar 51) to an

Owens–Wendt surface energy model as implemented in the Surface Energy Tool of the DropImage software. Optical images were taken with an Olympus BX41 microscope. $WO_3$ was electron beam evaporated from pellets (Sigma-Aldrich) using a Denton Explorer system. $WO_3$ was patterned for using lift-off using SPR3012 photoresist and patterned using photoplot masks using a Karl Suss MA-6 aligner. $SiO_2$ was patterned using a BMR Technology HiEtch ICP system using $CHF_3$ plasma.

## Acknowledgments

This work has been partially carried out at the Micro Device Laboratory (MDL) at Stevens Institute of Technology, funded with support from W15QKN-05-D-0011. This research project used microscopy resources, which was partially funded by the National Science Foundation via Grant DMR-0922522, within the Laboratory for Multiscale Imaging at Stevens Institute of Technology. The research was also carried out in part at the Center for Functional Nanomaterials, Brookhaven National Laboratory, which is supported by the US Department of Energy, Office of Basic Energy Sciences, under Contract No. DE-SC0012704. This work has also been partially supported by the Stanley Crooks Fellowship and NSF GK12 Fellowship.

## References

[1] Eda G and Maier S A 2013 Two-dimensional crystals: managing light for optoelectronics *ACS Nano* **7** 5660–5
[2] Gutiérrez H R, Perea-López N, Elías A L, Berkdemir A, Wang B, Lv R, López-Urías F, Crespi V H, Terrones H and Terrones M 2013 Extraordinary room-temperature photoluminescence in triangular $WS_2$ monolayers *Nano Lett.* **13** 3447–54
[3] Peimyoo N, Shang J, Cong C, Shen X, Wu X, Yeow E K L and Yu T 2013 Nonblinking, intense two-dimensional light emitter: monolayer $WS_2$ triangles *ACS Nano* **7** 10985–94
[4] Liu X, Hu J, Yue C, Della F N, Ling Y, Mao Z and Wei J 2014 High performance field-effect transistor based on multilayer tungsten disulfide *ACS Nano* **8** 10396–402
[5] Ovchinnikov D, Allain A, Huang Y, Dumcenco D and Kis A 2014 Electrical transport properties of single-layer $WS_2$ *ACS Nano* **8** 8174–81
[6] Kato T and Kaneko T 2014 Optical detection of a highly localized impurity state in monolayer tungsten disulfide *ACS Nano* **8** 12777–85
[7] Radisavljevic B, Radenovic A, Brivio J, Giacometti V and Kis A 2011 Single-layer $MoS_2$ transistors *Nat. Nanotechnol.* **6** 147–50
[8] Haigh S J, Gholinia A, Jalil R, Romani S, Britnell L, Elias D C, Novoselov K S, Ponomarenko L A, Geim A K and Gorbachev R 2012 Cross-sectional imaging of individual layers and buried interfaces of graphene-based heterostructures and superlattices *Nat. Mater.* **11** 764–7
[9] Gong Y *et al* 2014 Vertical and in-plane heterostructures from $WS_2/MoS_2$ monolayers *Nat. Mater.* **13** 1135–42
[10] Geim A K and Grigorieva I V 2013 Van der Waals heterostructures *Nature* **499** 419–25
[11] Petrone N, Dean C R, Meric I, van der Zande A M, Huang P Y, Wang L, Muller D, Shepard K L and Hone J 2012 Chemical vapor deposition-derived graphene with electrical performance of exfoliated graphene *Nano Lett.* **12** 2751–6
[12] Robinson J A, LaBella M, Zhu M, Hollander M, Kasarda R, Hughes Z, Trumbull K, Cavalero R and Snyder D 2011 Contacting graphene *Appl. Phys. Lett.* **98** 053103
[13] Tsai M-L, Su S-H, Chang J-K, Tsai D-S, Chen C-H, Wu C-I, Li L-J, Chen L-J and He J-H 2014 Monolayer $MoS_2$ heterojunction solar cells *ACS Nano* **8** 8317–22
[14] Slender C L, Greyson E C, Babayan Y and Odom T W 2005 Patterned $MoS_2$ nanostructures over centimeter-square areas *Adv. Mater.* **17** 2837–41
[15] Song I, Park C, Hong M, Baik J, Shin H J and Choi H C 2014 Patternable large-scale molybdenium disulfide atomic layers grown by gold-assisted chemical vapor deposition *Angew. Chem., Int. Ed.* **53** 1266–9
[16] Kim K S, Zhao Y, Jang H, Lee S Y, Kim J M, Kim K S, Ahn J-H, Kim P, Choi J-Y and Hong B H 2009 Large-scale pattern growth of graphene films for stretchable transparent electrodes *Nature* **457** 706–10
[17] Lee Y H and Lee J H 2009 Catalyst patterned growth of interconnecting graphene layer on $SiO_2$/Si substrate for integrated devices *Appl. Phys. Lett.* **95** 143102
[18] Liu Z *et al* 2013 In-plane heterostructures of graphene and hexagonal boron nitride with controlled domain sizes *Nat. Nanotechnol.* **8** 119–24
[19] Kim S J *et al* 2015 Ultraclean patterned transfer of single-layer graphene by recyclable pressure sensitive adhesive films *Nano Lett.* **15** 3236–40
[20] Choi J, Kwak J, Park S, Yun H D, Kim S and Jung M 2015 Growth of wrinkle-free graphene on texture-controlled platinum films and thermal-assisted transfer of large-scale patterned graphene *ACS Nano* **9** 679–86
[21] Cong C, Shang J, Wu X, Cao B, Peimyoo N, Qiu C, Sun L and Yu T 2014 Synthesis and optical properties of large-area single-crystalline 2D semiconductor $WS_2$ monolayer from chemical vapor deposition *Adv. Opt. Mater.* **2** 131–6
[22] Rong Y, He K, Pacios M, Robertson A W, Bhaskaran H and Warner J H 2015 Controlled preferential oxidation of grain boundaries in monolayer tungsten disulfide for direct optical imaging *ACS Nano* **9** 3695–703
[23] Zhang Y *et al* 2013 Controlled growth of high-quality monolayer $WS_2$ layers on sapphire and imaging its grain boundary *ACS Nano* **7** 8963–71
[24] Elías A L *et al* 2013 Controlled synthesis and transfer of large-area $WS_2$ sheets: from single layer to few layers *ACS Nano* **7** 5235–42
[25] Park J, Lee W, Choi T, Hwang S-H, Myoung J M, Jung J-H, Kim S-H and Kim H 2014 Layer-modulated synthesis of uniform tungsten disulfide nanosheet using gas-phase precursors *Nanoscale* **7** 1308–13
[26] Jeon J, Jang S K, Jeon S M, Yoo G, Park J and Lee S 2015 Controlling grain size and continuous layer growth in two-dimensional $MoS_2$ films for nanoelectronic device application *IEEE Trans. Nanotechnol.* **14** 238
[27] Yang J, Kim S, Choi W, Park S H, Jung Y, Cho M H and Kim H 2013 Improved growth behavior of atomic-layer-deposited high-k dielectrics on multilayer $MoS_2$ by oxygen plasma pretreatment *ACS Appl. Mater. Interfaces* **5** 4739–44
[28] George A S, Mutlu Z, Ionescu R, Wu R J, Jeong J S, Bay H H, Chai Y, Mkhoyan K A, Ozkan M and Ozkan C S 2014 Wafer scale synthesis and high resolution structural characterization of atomically thin $MoS_2$ layers *Adv. Funct. Mater.* **24** 7461–6
[29] Kang K, Xie S, Huang L, Han Y, Huang P Y, Mak K F, Kim C-J, Muller D and Park J 2015 High-mobility three-atom-thick semiconducting films with wafer-scale homogeneity *Nature* **520** 656–60

[30] Yu Y, Li C, Liu Y, Su L, Zhang Y and Cao L 2013 Controlled scalable synthesis of uniform, high-quality monolayer and few-layer $MoS_2$ films *Sci. Rep.* **3** 1866

[31] Huang J K, Pu J, Hsu C L, Chiu M H, Juang Z Y, Chang Y H, Chang W H, Iwasa Y, Takenobu T and Li L J 2014 Large-area synthesis of highly crystalline $WSe_2$ monolayers and device applications *ACS Nano* **8** 923–930

[32] Yun S J *et al* 2015 Synthesis of centimeter-scale monolayer tungsten disulfide film on gold foils *ACS Nano* **9** 5510–9

[33] Gao Y *et al* 2015 Large-area synthesis of high-quality and uniform monolayer $WS_2$ on reusable Au foils *Nat. Commun.* **6** 8569

[34] Bertolazzi S, Krasnozhon D and Kis A 2013 Nonvolatile memory cells based on MoS2/graphene heterostructures *ACS Nano* **7** 3246–52

[35] Fuhrer M S and Hone J 2013 Measurement of mobility in dual-gated $MoS_2$ transistors *Nat. Nanotechnol.* **8** 146–7

[36] Jin T, Kang J, Su Kim E, Lee S and Lee C 2013 Suspended single-layer $MoS_2$ devices *J. Appl. Phys.* **114** 164509

[37] Lopez-Sanchez O, Lembke D, Kayci M, Radenovic A and Kis A 2013 Ultrasensitive photodetectors based on monolayer $MoS_2$ *Nat. Nanotechnol.* **8** 497–501

[38] Wang H, Yu L, Lee Y-H, Shi Y, Hsu A, Chin M L, Li L-J, Dubey M, Kong J and Palacios T 2012 Integrated circuits based on bilayer $MoS_2$ transistors *Nano Lett.* **12** 4674–80

[39] Radisavljevic B, Whitwick M B and Kis A 2011 Integrated circuits and logic operations based on single-layer $MoS_2$ *ACS Nano* **5** 9934–8

[40] Zhu Z Y, Cheng Y C and Schwingenschlögl U 2011 Giant spin-orbit-induced spin splitting in two-dimensional transition-metal dichalcogenide semiconductors *Phys. Rev.* B **84** 153402

[41] Liu L, Kumar S B, Ouyang Y and Guo J 2011 Performance limits of monolayer transition metal dichalcogenide transistors *IEEE Trans. Electron Devices* **58** 3042–7

[42] Bernardi M, Palummo M and Grossman J C 2013 Extraordinary sunlight absorption and one nanometer thick photovoltaics using two-dimensional monolayer materials *Nano Lett.* **13** 3664–70

[43] Ye Z, Cao T, O'Brien K, Zhu H, Yin X, Wang Y, Louie S G and Zhang X 2014 Probing excitonic dark states in single-layer tungsten disulphide *Nature* **513** 214–8

[44] He Z, Xu W, Zhou Y, Wang X, Sheng Y, Rong Y, Guo S, Zhang J, Smith J M and Warner J H 2016 Biexciton formation in bilayer tungsten disulfide *ACS Nano* **10** 2176–83

[45] Currie M, Hanbicki A T, Kioseoglou G and Jonker B T 2015 Optical control of charged exciton states in tungsten disulfide *Appl. Phys. Lett.* **106** 201907

[46] Boulesbaa A *et al* 2015 Observation of two distinct negative trions in tungsten disulfide monolayers *Phys. Rev.* B **92** 1–7

[47] Hanbicki A T, Currie M, Kioseoglou G, Friedman A L and Jonker B T 2015 Measurement of high exciton binding energy in the monolayer transition-metal dichalcogenides $WS_2$ and $WSe_2$ *Solid State Commun.* **203** 16–20

[48] Ye Y, Wong Z J, Lu X, Ni X, Zhu H, Chen X, Wang Y and Zhang X 2015 Monolayer excitonic laser *Nat. Photonics* **9** 733–737

[49] Rasband W S 1997–2016 *ImageJ* (Bethesda, MD: U. S. National Institutes of Health) (http://imagej.nih.gov/ij/)

[50] Ly T H *et al* 2014 Observing grain boundaries in CVD-grown monolayer transition metal dichalcogenides *ACS Nano* **8** 11401–8

[51] Owens D K and Wendt R C 1969 Estimation of the surface free energy of polymers *J. App. Poly. Sci.* **13** 1741–7

[52] Liu X M, Thomason J L and Jones F R 2009 The concentration of hydroxyl groups on glass surfaces and their effect on the structure of silane deposits *Silanes and Other Coupling Agents* vol 5 ed K L Mittal (Leiden: Koninklijke Brill NV) pp 25–38

[53] Liberelle B, Banquy X and Giasson S 2008 Stability of silanols and grafted alkylsilane monolayers on plasma-activated mica surfaces *Langmuir* **24** 3280–8

[54] Chen C, Zhang N, Li W and Song Y 2015 Water contact angle dependence with hydroxyl functional groups on silica surfaces under $CO_2$ sequestration conditions *Environ. Sci. Technol.* **49** 14680–7

[55] Bhattacharya S, Datta A, Berg J M and Gangopadhyay S 2005 Studies on surface wettability of poly(dimethyl) siloxane (PDMS) and glass under oxygen-plasma treatment and correlation with bond strength *J. Microelectromech. Syst.* **14** 590–7

[56] Preston D J, Miljkovic N, Sack J, Enright R, Queeney J and Wang E N 2014 Effect of hydrocarbon adsorption on the wettability of rare earth oxide ceramics *Appl. Phys. Lett.* **105** 011601

[57] Iglauer S, Salamah A, Sarmadivaleh M, Liu K and Phan C 2014 Contamination of silica surfaces: impact on water-$CO_2$-quartz and glass contact angle measurements *Int. J. Greenh. Gas Control* **22** 325–8

[58] Kim K D, Tai W S, Kim Y D, Cho S J, Bae I S, Boo J H, Lee B C, Yang K H and Park O K 2009 Change in water contact angle of carbon contaminated $TiO_2$ surfaces by high-energy electron beam *Bull. Korean Chem. Soc.* **30** 1067–70

[59] Alam A U, Howlader M M R and Deen M J 2014 The effects of oxygen plasma and humidity on surface roughness, water contact angle and hardness of silicon, silicon dioxide and glass *J. Micromech. Microeng.* **24** 035010

[60] DeYoreo J J and Vekilov P G 2003 Principles of crystal nucleation and growth *Rev. Mineral. Geochem.* **54** 57–93

[61] Lassner E and Schubert W D 1999 Tungsten: properties, chemistry, technology of the element, alloys, and chemical compounds (New York: Springer) ch 3

[62] Wykoff R W G 1931 *Structure of Crystals* 2nd edn (New York: Chemical Catalog Co.) p 233 and 239 (as interpreted into the file 5910003.cif from the Crystallographic Open Database)

[63] Berkdemir A *et al* 2013 Identification of individual and few layers of $WS_2$ using Raman spectroscopy *Sci. Rep.* **3** 1755

[64] Horcas I, Fernandez R, Gomez-Rodriguez J M, Colchero J, Gomez-Herrero J and Baro A M 2007 WSXM: A software for scanning probe microscopy and a tool for nanotechnology *Rev. Sci. Instr.* **78** 013705 (wsxmsolutions.com)